Electrically-Tunable Compact Thin-Film Magnetoelectric Resonators

Amal El-Ghazaly[1], Joseph T. Evans[2], Noriyuki Sato[1], Naomi Montross[2], Hendrik Ohldag[3], Robert M. White[4], and Shan X. Wang[1,4]

[1]Electrical Engineering, Stanford University, Stanford, CA 94305 USA
[2]Radiant Technologies, Inc., Albuquerque, NM 87107 USA
[3]Stanford Synchrotron Radiation Laboratory, SLAC, Menlo Park, California 94025 USA
[4]Materials Science and Engineering, Stanford University, Stanford, CA 94305 USA

Abstract

Magnetoelectrics have attracted much attention for their ability to control magnetic behavior electrically and electrical behavior magnetically. This feature provides numerous benefits to electronic systems and can potentially serve as the bridge needed to integrate magnetic devices into mainstream electronics. Here, we pursue this natural next step and produce thin-film integrated magnetoelectric devices for radio frequency electronics. These devices provide electric field control of magnetic permeability in order to change the resonance frequency of coplanar waveguides. Over the course of this study, the various thin-film material phenomenon, trade-offs, and integration considerations for multi-phase magnetoelectrics are analyzed and discussed. The fabricated devices achieved reversible tunability of the resonance frequency, characterized by a converse magnetoelectric coupling coefficient of up to 24 mG-cm/V.

The ability to electrically control magnetic materials is highly sought after as applications for magnetic devices in integrated electronics continue to increase. Voltage control of magnetism has already proved advantageous for a variety of device industries, including sensors and actuators [1, 2], computational memory and logic systems [3–5], and inductors and transformers [6, 7]. In each of these cases, an electric field applied to the device couples either directly or indirectly to the magnetization and changes its state. This magnetoelectric coupling property can be found in single-phase multiferroic materials (those exhibiting both ferroelectricity and ferromagnetism) or multi-phase material systems (combining different types of ferroic materials into composites). In this work, we develop a thin-film, two-phase magnetoelectric system and integrate it in the form of a waveguide resonator in order to extend the reach of magnetoelectrics into yet another field - that of tunable wireless communication.

To avoid congestion of wireless communication channels, wireless electronics must be able to be tuned broadly across multiple channels, while also maintaining small form factors for portability. Various methods have been proposed for broadband tunability, mostly involving variable capacitors or inductors in resonant circuits [6, 9–12]. Resonators can also take other forms, such as waveguides, which can be tuned by changing either their effective capacitance [13] or effective inductance. Common drawbacks of many of these previous methods are their incompatibility with semiconductor circuit integration, bulk size, or limited tunability range. In this work, we explore the design and integration of thin-film magnetoelectrics for tunable coplanar waveguide resonators. These devices aim to satisfy semiconductor integration requirements while simultaneously providing large tunability by means of electrical control of magnetization.

We designed the tunable resonator device shown in Fig. 1 as a radio frequency (RF) quarter-wavelength resonator, whose resonance is based on the effective permeability and permittivity

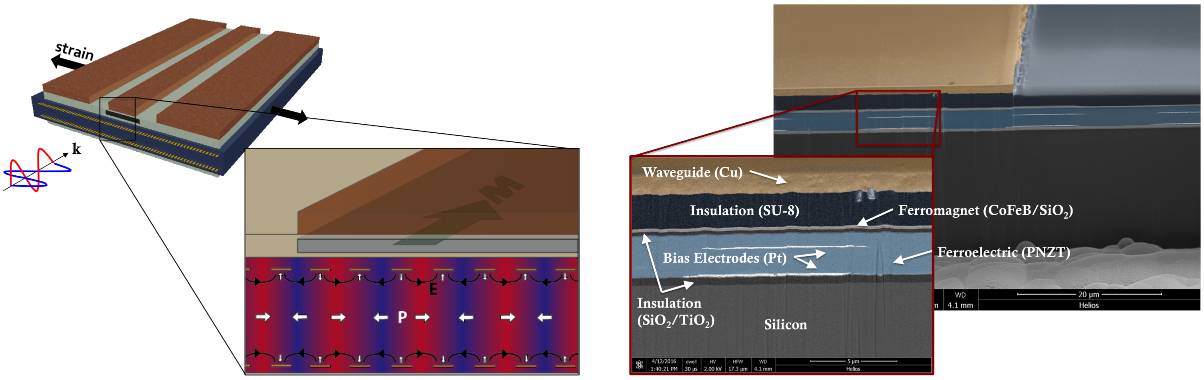

(a) (b)

Figure 1: Models and cross-sectional views of the magnetoelectric resonant waveguides: a) simplified 3D model of the magnetoelectric coplanar waveguide device indicating the axis of desired uniaxial tensile strain and the wave propagation direction. In addition, a simplified cross-sectional illustration of the material stack for the device, indicating the magnetization direction, polarization distribution, and electric field pattern. Layers are not to scale. b) Focused ion beam cross-sectional image of the fabricated device.

of the material stack. For tunability of the resonance frequency, we utilize a two-phase magnetoelectric in which the magnetic permeability can be varied through electric field control of strain. A coplanar waveguide on the surface of the structure carries the wave such that its propagation is influenced by the underlying magnetoelectric stack. The magnetoelectric is composed of a magnetostrictive ferromagnetic layer on top of a piezoelectric/electrodes combined layer, with the silicon substrate on the bottom. Figure 1a illustrates the simplified integrated structure as well as the magnetoelectric vectors of magnetization direction in the magnetic layer and polarization distribution in the piezoelectric layer. Figure 1b shows scanning electron microscope images of the cross-section of the fabricated devices, produced by focused-ion beam. Details of the fabrication process are presented in the Methods section.

While single-phase multiferroic materials offer the simplicity of a direct relationship between electric field and magnetization, their magnetoelectric coupling is generally confined to low temperatures [14–16] or epitaxial material systems [17–19]. Multi-phase magnetoelectrics, on the other hand, have the advantage of offering sufficient flexibility in design such that many can be produced to operate at room temperature [20] and a large number do not require epitaxial growth, particularly if the magnetoelectric coupling is produced via strains in the films [1, 21]. However, for strain-mediated magnetoelectrics, difficulties in the thin-film piezoelectric fabrication have limited work thus far to proof-of-concept demonstrations of magnetic films on bulk piezoelectric substrates rather than compact integrated devices. Recently, deposition of either sputtered AlN [2, 22] or sol-gel PZT [23] thin-film piezoelectrics have enabled preliminary progress into integrated films of magnetoelectric devices.

The previous demonstrations of thin-film piezoelectrics maximized strain and magnetoelectric coupling by mechanically releasing the films from the substrate. This approach, however, requires very large features to allow for backside release in select areas and reverts back to the similar challenges of integrating MEMS structures with other semiconductor devices. In addition, to simplify fabrication, often a parallel plate capacitor structure (vertically-stacked electrodes of opposite polarity sandwiching the piezoelectric film) is used, but this limits the actuator to biaxial strain related to the d_{31} piezoelectric coefficient, which is much smaller than the preferred d_{33} uniaxial piezoelectric coefficient. In contrast, in this work, we designed compact, integrated thin-film magnetoelectrics that utilize interdigitated electrodes (IDE) [24] to apply an in-plane electric field and take advantage of the larger d_{33} strains, as shown in Fig. 1a. In this way, we improve uniaxial control of the magnetic film properties without the need for backside release from the substrate.

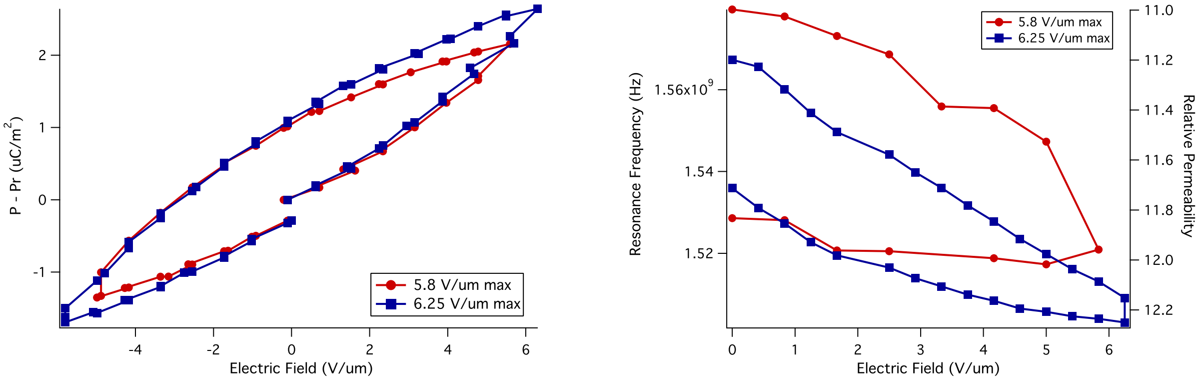

(a) (b)

Figure 2: Device results, including: a) Polarization hysteresis loops as a function of electric field, and b) quarter-wavelength resonance frequency sweep results as a function of electric field, described both in terms of frequency and relative permeability. Measurements are from separate devices.

We selected the ferromagnetic material $Co_{43}Fe_{43}B_{14}$ (At%) [25] for its high magnetostriction value of $\lambda_s \sim 55 \times 10^{-6}$ and high ferromagnetic resonance frequency ($\sim$ 2 GHz for a square film). In addition, the magnetic film was laminated (see Methods section) and patterned into a narrow bar parallel to the wave propagation direction, such that the shape anisotropy contributes to aligning the magnetization uniformly along the length direction, with permeability measured along the orthogonal (width) direction. For the ferroelectric material, we selected sol-gel Niobium-doped lead zirconate titanate (4/20/80 PNZT) for its higher piezoelectric linearity compared to regular sol-gel PZT. The ferroelectric was poled in-plane using the IDE prior to measurements of the resonance tunability such that the initial polarization was distributed as shown in Fig. 1a.

Figure 2 presents measurement results from the magnetoelectric resonator device. Minor-loop polarization measurements around the remanence point are shown in Fig. 2a, indicating that the polarization and corresponding strain (not shown) is fairly linear and reversible, despite a degree of hysteresis. The corresponding RF resonance shifts for the magnetoelectric device after poling are given in Fig. 2b. The quarter wavelength resonance point of the waveguides appears at a frequency corresponding to the following equation related to the magnetic material's permeability:

$$f_{\frac{\lambda}{4}} = \frac{1}{4l\sqrt{\mu\epsilon}}. \tag{1}$$

The right axis of Fig. 2b marks the calculated permeability values based on the assumption that the permeability of the magnetic material and permittivity ($\sim$ 3.2) of the surrounding thick dielectric (SU-8) dictate the phase velocity of the wave. As an electric field is applied to the piezoelectric, it transfers stress to the magnet, which decreases the effective anisotropy and increases the magnetic permeability. This outcome corresponds to a decrease in the resonance frequency of the waveguide. Both the polarization and resonance frequency results demonstrate that as the electric field is swept out to a given maximum value and returned back to zero, the polarization increases then decreases and the resonance frequency decreases then increases, as expected. The hysteresis observed in each polarization sweep is reflected in the frequency response as "hysteresis" in the resonance shift.

In order to verify whether the frequency shifts are truly due to magnetic anisotropy changes in the magnetoelectric stack, we directly measured the shift in ferromagnetic resonance (FMR) frequency with applied electric field during the poling process, as plotted in Fig. 3. The values for $H_{k_{eff}}$, shown on the second axis, were calculated by fitting the FMR measurement results to the Kittel equation [29] and extracting its shift with applied electric field (additional information is provided in Supplementary Information). The graph confirms a decrease in the anisotropy

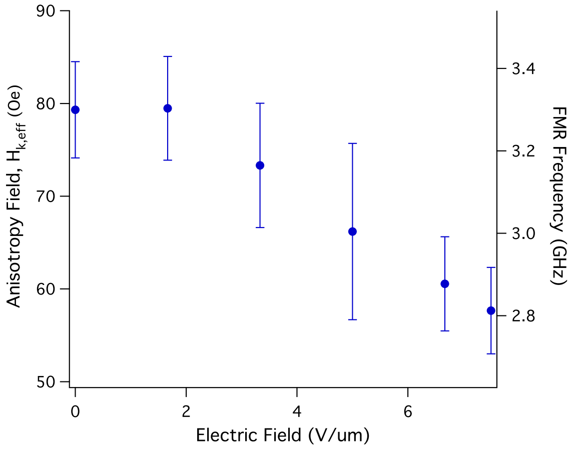

Figure 3: Ferromagnetic resonance frequency and anisotropy shift: Fitted results to the FMR frequency measurement as a function of applied electric field. The effective anisotropy field was extracted by fitting to the Kittel equation using MATLAB. Error bars indicate the 68% confidence interval.

field by more than 20 Oe as the electric field is increased from zero to 7.5 V/μm, indicating that the magnetoelectric coupling in the device is quite strong. In addition, the results verify that the FMR frequency is far beyond the quarter wavelength resonance frequency of the waveguide, thereby providing sufficient separation between the permeability peak at the FMR frequency and the tunable resonance frequency of the guide itself.

From the resonance measurements in Fig. 2b, we can evaluate the linear shift in $H_{k_{eff}}$ to be in the range of 10 Oe (5 Oe of which are reversible) for an applied field of 6.25 V/μm. Neglecting contributions due to stray fields or temperature effects, we can extract an effective magnetoelectric coefficient for the composite device equal to approximately 24 mG-cm/V.

Not shown in Fig. 2b are the tunability results under negative applied electric fields, which experimentally mirror the positive field behavior. Considering that the polarization in Fig. 2a decreases for negative fields, the strain would be expected to contract and cause the resonance frequency to increase instead of decreasing. The peculiarity of the experimental behavior can be attributed to two possible reasons: the field-squared behavior of strain in non-switching domains and the intense localization of the stresses and strains due to substrate clamping. In the first case, since the applied field is not large enough to switch the remanent polarization, the low-field strain behavior follows the square of the applied field, as in most piezoelectric butterfly loops. In support of the latter case, the COMSOL Multiphysics simulations in Fig. 4 suggest that, as a result of substrate clamping, the strains transferred to the magnetic layer are due to bending at or near the interdigitated electrode with positive polarity. When a negative voltage is applied, the stress appears to merely shift to the adjacent electrode, but the device maintains the same net behavior of decreasing the resonance frequency. However, due to the very localized and complicated stress arrangement near the electrodes, other than predicting general rotation of the magnetization, the finer details of the magnetization response are non-trivial to predict.

In addition, both the magnetic and ferroelectric domain images in Fig. 5 imply complexity of the thin film material responses to the non-uniform stress. While the ferromagnetic thin film was found to be uniformly magnetized as a single domain, defects in the film result in non-ideal magnetization behavior. Furthermore, the non-poled piezoresponse force microscope (PFM) images in Fig. 5b illustrate the randomness of the initial, non-poled ferroelectric domains that govern the underlying behavior of the thin-film ferroelectric. When a saturating electric field is applied, the domains of the ferroelectric sporadically rotate to align with the field in a nonlinear fashion, depending on each domain's electrical coercivity [28]. Once fully poled, as in Fig. 5c, the behavior becomes more linear and reversible, with the exception of small hysteretic behavior in the ferroelectric at remanence (Fig. 2a). Nevertheless, a certain degree of randomness from

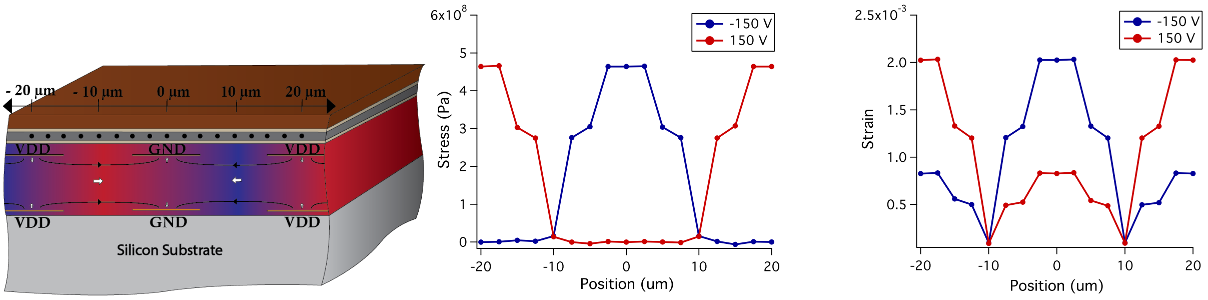

(a) (b) (c)

Figure 4: COMSOL stress and strain simulation results: a) Model of the section of the simplified stack cross-section used in the COMSOL simulations. Points used for evaluation of stress and strain are marked by dots in the center of the magentic layer. b) Stress and c) strain as a function of position at each of the points marked in a).

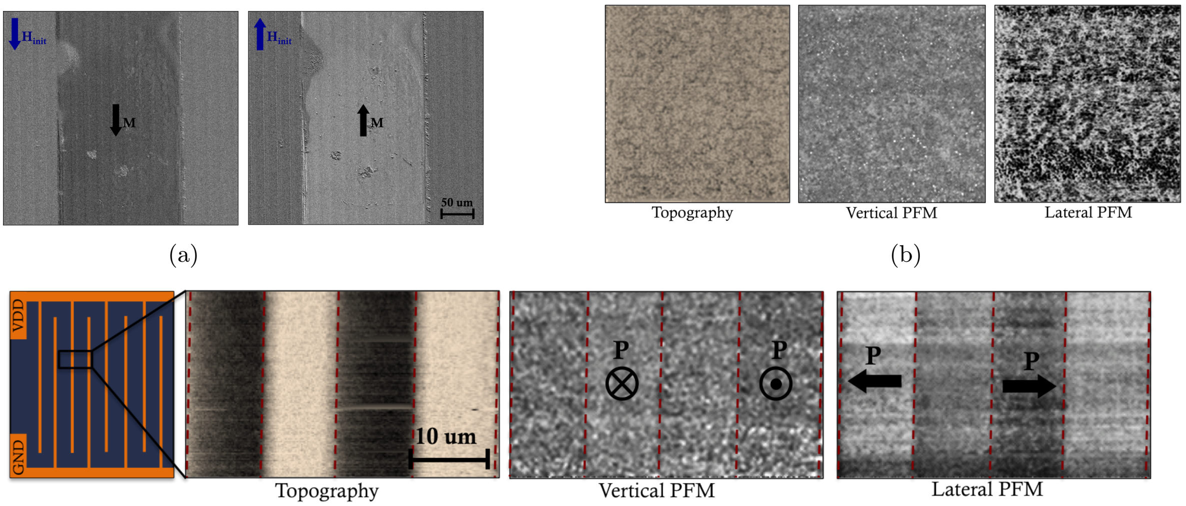

(c)

Figure 5: Magnetic and piezoelectric domain images: a) Magneto-Optic Kerr Effect microscopy images illustrating the single-domain nature of the long magnetic bars, with the exception of defects. PFM images b) prior to poling and c) of the poled device (including electrodes). From left to right, each set includes a topography image, vertical-sensitivity PFM image, and lateral-sensitivity PFM image to illustrate the directionality of the piezoelectric domains.

the small domains may influence the final device behavior.

The goal of this work was to explore new thin-film magnetoelectric capabilities in a realistic, fully-integrated RF device. Here, we have demonstrated a thin-film, compact, integrated magnetoelectric resonator for tunable RF wireless communication. The design of the device takes into account practical semiconductor integration considerations while simultaneously achieving large tunability sufficient for hopping across communication channels that are typically 20 MHz wide in frequency. With a reversible magnetoelectric coefficient of 24 mG-cm/V, these devices represent promising and exciting steps toward magnetoelectric device integration for electrical control of magnetization in future integrated systems. Future research endeavors may attempt to achieve greater strains and magnetoelectric coupling through a number of methods: releasing the structures from the substrate to eliminate clamping; utilizing thicker piezoelectric films to allow the piezoelectric, rather than the stiffer magnetic film, to dominate the elastic behavior; and, selecting a magnetic material with a lower Young's modulus. Finally, to make these devices more practical for portable electronic systems, lower voltages would be necessary. This can be done with either reducing the magnetic anisotropy in order to increase its magnetomechanical coupling [26] or by reducing the electrode spacing to maintain the strength of the electric field but at lower operating voltages. With these optimizations, we have no doubt that future integrated magnetoelectrics may have a significant role to play in tunable RF wireless electronics.

Methods

Device Fabrication

The first half of the magnetoelectric waveguide fabrication process (fabrication of the piezoelectric and interdigitated electrode process) was completed at Radiant Technologies, Inc., while the second half (fabrication of the magnet and waveguide) was completed at Stanford University. First, thermal SiO_2, ranging from 200 to 500 nm in thickness, was grown on a Si wafer ($\sim 500\mu$m thick). Then, a thin layer of thermal TiO_2 was deposited as a diffusion barrier between the bottom electrodes and the underlying SiO_2 layer. The wafer was patterned with photoresist for the inverse of the bottom electrode pattern and 150 nm of Pt was deposited by e-beam evaporation. The photoresist was immediately removed after the deposition, leaving behind the Pt bottom electrode. (This is called a lift-off process.) Sol-gel PNZT (4/20/80) was spun onto the wafer in multiple layers. Each layer was calcined at 450°C and the wafer was sintered at 650°C after every third layer. This process was repeated until the desired 2 μm thickness of PNZT was achieved. The 100 nm Pt top electrode was deposited and patterned just as the bottom electrode, using a lift-off process. Another 0.7 μm of PNZT was spun, calcined, and sintered above the top electrode. The full PNZT was etched to pattern the film and open up vias to the bottom and top electrodes. A 600 nm inert passivation layer of TiO_2 and SiO_2 was deposited above the structures and etch to, once again, open the vias to the electrodes.

The magnetic film was deposited in the form of laminations, which are used to break up eddy currents and help to reduce losses at high frequencies. The laminated $Co_{43}Fe_{43}B_{14}$ (At%) magnetic film was deposited using RF sputtering and patterned using lift-off. The lamination process alternated deposition between sputtering the CoFeB (66 nm) and SiO_2 (6 nm) in the same chamber. A total film thickness of 250 nm (4 layers) was used. To prevent the conductive magnetic material from short-circuiting the coplanar waveguide, a 1 μm-thick insulating layer of photosensitive SU-8 type 2002 was spun onto the wafer and patterned using photolithography. The 500 nm thick Cu coplanar waveguide was deposited using e-beam evaporation and patterned using a lift-off process. Finally, 50 nm of SiO_2 were deposited over the entire wafer to prevent oxidation and degradation of the device over time.

Samples were diced and bonded to chip carriers. Wirebonds were made between the metallized bondpads for the IDE and the pads of the chip carrier. These connections were used to apply voltage to the IDE during testing, while the waveguide was separately probed.

Resonance Frequency Evaluation

The quarter wavelength resonance point is characterized by a change in the input impedance of the waveguide corresponding to:

$$Z_{in} = \frac{Z_0^2}{Z_L} \quad at\ f = \frac{\lambda}{4} \tag{2}$$

where Z_0 is the characteristic impedance of the line. For simplicity of analysis we fabricated both short-circuit terminated ($Z_L = 0$) and open-circuit terminated ($Z_L = \infty$) waveguides, which at quarter-wavelength resonance appear as the opposite impedance from the input.

The waveguides were probed at the input using 200 μm-pitch ground-signal-ground (GSG) probes, which connected to an Agilent 8753ES network analyzer. The change in the input impedance was evaluated after extracting the real and imaginary parts of the S11 scattering parameter. In the case of a single-port measurement, this S11 parameter can be approximated as the reflection coefficient at the input of the device. While the magnitude of the reflection coefficient, $|\Gamma|$, is ideally equal to 1 for both short and open-circuited lines, the phase rotates from 0° to 180° when the input impedance changes from open to short, respectively, and vice versa. The magnitude and phase of the reflection coefficient are calculated using the following equations:

$$|\Gamma| = \sqrt{Re(\Gamma)^2 + Im(\Gamma)^2} \tag{3}$$

$$\angle\Gamma = \frac{Im(\Gamma)}{Re(\Gamma)} \tag{4}$$

Results reported in this paper are all from open-circuited waveguides. Therefore, the quarter wavelength resonance frequency was interpolated as the point at which the phase ($\angle\Gamma$) was equal to 180°.

FMR Measurement and Fitting

In order to extract the effective anisotropy field, $H_{k_{eff}}$, the ferromagnetic resonance was measured using a magnetic-field sweep method described in [30]. The FMR frequency as a function of DC magnetic field was measured at each applied electric field. Then, the data for each FMR sweep (at a single electric field value) was fitted in MATLAB to the following form of the Kittel equation:

$$\omega_{FMR} = \gamma\sqrt{(H_{k_{eff}} + H_{DC} + 4\pi N_y M_s)(H_{k_{eff}} + H_{DC} + 4\pi N_z M_s)} \tag{5}$$

where N_y is the demagnetization factor along the hard axis of the magnet (width direction of the waveguide), N_z is the demagnetization factor in the thickness direction, and H_{DC} is the applied DC magnetic field. This equation assumes that the demagnetization factor along the easy axis (8 mm length direction of the waveguide) is equivalent to zero.

Effective Electrode Area and Spacing Calculation

In order to evaluate the polarization, the electrode area needed to be known. Since the thickness of the electrodes are much smaller than the width of the electrodes, we ignore the thickness dimension in the area calculation and instead only sum the area on the top surface of the bottom electrode, and both the bottom and top surfaces of the top electrode. This resulted in a total electrode area of 0.093 cm^2 for the magnetoelectric composite device.

In order to calculate the applied electric field values from the known applied voltage, the length of the field lines between electrodes was required ($E \sim \frac{V}{d}$). We approximate that the field lines travel vertically halfway into the thickness of the piezoelectric, then across the spacing between electrodes, and vertically back to the next electrode. This length is evaluated as the electrode spacing (10 μm) plus half of the thickness of the piezoelectric sandwiched between the electrodes (1 μm) on both sides of the electrode gap, such that the total length of the field line is 12 μm. The electric fields calculated using this length were compared to those in the COMSOL simulations and found to give a fairly good approximation of the actual electric field values.

Magnetoelectric Coefficient Calculation

The converse magnetoelectric effect (CME) describes the change in magnetization due to electric field (as opposed to change in polarization due to magnetic field in the case of the regular magnetoelectric effect). Since the effective anisotropy field relates to the magnetization through the susceptibility $M = \chi H_{k_{eff}}$, we evaluated the change in magnetization from the change in effective anisotropy field using the following equation:

$$\alpha_{CME} = \frac{4\pi dM}{dE} = \frac{4\pi \chi H_{k_{eff}}}{dE} \quad \textit{in cgs units} \tag{6}$$

Acknowledgment

The authors would like to thank Bastiaan Bergman of Western Digital Corporation for his help with the measurement of magnetostriction constants. They would also like to thank Satoru Emori and Professor Yuri Suzuki's research group at Stanford University for their help with the FMR measurements. Research for this project was conducted with government support under FA9550-11-C-0028 and awarded by the Department of Defense, Air Force Office of Scientific Research, National Defense Science and Engineering Graduate (NDSEG) Fellowship, 32 CFR 168a. Part of this work was performed using the Stanford Nanofabrication Facility (SNF) and the Stanford Nano Shared Facilities (SNSF) at Stanford University.

References

[1] C. Israel, N. D. Mathur, and J. F. Scott, "A one-cent room-temperature magnetoelectric sensor," *Nature materials*, vol. 7, no. February, pp. 93–94, 2008.

[2] H. Greve, E. Woltermann, H.-J. Quenzer, B. Wagner, and E. Quandt, "Giant magnetoelectric coefficients in (Fe90Co10)78Si12B10-AlN thin film composites," *Applied Physics Letters*, vol. 96, no. 18, p. 182501, 2010. [Online]. Available: http://link.aip.org/link/APPLAB/v96/i18/p182501/s1&Agg=doi

[3] M. Bibes and A. Barthélémy, "Multiferroics: towards a magnetoelectric memory," *Nature materials*, vol. 7, no. June, pp. 425–426, 2008.

[4] G. Yu, Z. Wang, M. Abolfath-Beygi, C. He, X. Li, K. L. Wong, P. Nordeen, H. Wu, G. P. Carman, X. Han, I. A. Alhomoudi, P. K. Amiri, and K. L. Wang, "Strain-induced modulation of perpendicular magnetic anisotropy in Ta/CoFeB/MgO structures investigated by ferromagnetic resonance," *Applied Physics Letters*, vol. 106, no. 7, p. 072402, 2015.

[5] J. F. Scott, "Multiferroic memories," *Nature Materials*, vol. 6, no. April, pp. 256–257, 2007.

[6] J. Lou, D. Reed, M. Liu, and N. X. Sun, "Electrostatically tunable magnetoelectric inductors with large inductance tunability," *Applied Physics Letters*, vol. 94, no. 11, p. 112508, 2009. [Online]. Available: http://link.aip.org/link/APPLAB/v94/i11/p112508/s1&Agg=doi

[7] S. Dong, J. Zhai, S. Priya, J.-F. Li, and D. Viehland, "Tunable features of magnetoelectric transformers," *IEEE transactions on ultrasonics, ferroelectrics, and frequency control*, vol. 56, no. 6, pp. 1124–7, jul 2009. [Online]. Available: http://www.ncbi.nlm.nih.gov/pubmed/19574118

[8] A. R. Brown and G. M. Rebeiz, "A Varactor-Tuned RF Filter," *IEEE Transactions on Microwave Theory and Techniques*, vol. 48, no. 7, pp. 1157–1160, 2000.

[9] M. Rais-zadeh, P. A. Kohl, and F. Ayazi, "MEMS Switched Tunable Inductors," *Journal of Microelectromechanical Systems*, vol. 17, no. 1, pp. 78–84, 2008.

[10] P. Andreani and S. Mattisson, "On the use of MOS varactors in RF VCO's," *IEEE Journal of Solid-State Circuits*, vol. 35, no. 6, pp. 905–910, 2000.

[11] M. Vroubel, Y. Zhuang, B. Rejaei, and J. Burghartz, "Integrated Tunable Magnetic RF Inductor," *IEEE Electron Device Letters*, vol. 25, no. 12, pp. 787–789, dec 2004. [Online]. Available: http://ieeexplore.ieee.org/lpdocs/epic03/wrapper.htm?arnumber=1362775

[12] J. Salvia, J. A. Bain, and C. P. Yue, “Tunable on-chip inductors up to 5 GHz using patterned permalloy laminations,” vol. 00, no. 1, 2005, pp. 963–966.

[13] W. H. Woods, A. Valdes-Garcia, H. Ding, and J. Rascoe, “CMOS millimeter wave phase shifter based on tunable transmission lines,” no. 3, 2013, pp. 1–4. [Online]. Available: http://ieeexplore.ieee.org/lpdocs/epic03/wrapper.htm?arnumber=6658442

[14] S.-W. Cheong and M. Mostovoy, “Multiferroics: a magnetic twist for ferroelectricity,” *Nature Materials*, vol. 6, no. 1, pp. 13–20, 2007. [Online]. Available: http://www.nature.com/doifinder/10.1038/nmat1804

[15] R. Ramesh and N. A. Spaldin, “Multiferroics: progress and prospects in thin films,” *Nature Materials*, vol. 6, no. 1, pp. 21–29, 2007. [Online]. Available: http://www.nature.com/doifinder/10.1038/nmat1805

[16] T. Fix, E. M. Choi, J. W. A. Robinson, S. B. Lee, A. Chen, B. Prasad, H. Wang, M. G. Blamire, and J. L. Macmanus-Driscoll, “Electric-field control of ferromagnetism in a nanocomposite via a ZnO phase,” *Nano Letters*, vol. 13, no. 12, pp. 5886–5890, 2013.

[17] Y.-H. Chu, L. W. Martin, M. B. Holcomb, M. Gajek, S.-J. Han, Q. He, N. Balke, C.-H. Yang, D. Lee, W. Hu, Q. Zhan, P.-L. Yang, A. Fraile-Rodríguez, A. Scholl, S. X. Wang, and R. Ramesh, “Electric-field control of local ferromagnetism using a magnetoelectric multiferroic.” *Nature Materials*, vol. 7, no. 6, pp. 478–82, jun 2008. [Online]. Available: http://www.ncbi.nlm.nih.gov/pubmed/18438412

[18] J. Wang, J. B. Neaton, H. Zheng, V. Nagarajan, S. B. Ogale, B. Liu, D. Viehland, V. Vaithyanathan, D. G. Schlom, U. V. Waghmare, N. a. Spaldin, K. M. Rabe, M. Wuttig, and R. Ramesh, “Epitaxial BiFeO3 multiferroic thin film heterostructures.” *Science*, vol. 299, no. 5613, pp. 1719–1722, 2003.

[19] T. Zhao, A. Scholl, F. Zavaliche, K. Lee, M. Barry, A. Doran, M. P. Cruz, Y. H. Chu, C. Ederer, N. a. Spaldin, R. R. Das, D. M. Kim, S. H. Baek, C. B. Eom, and R. Ramesh, “Electrical control of antiferromagnetic domains in multiferroic BiFeO3 films at room temperature.” *Nature materials*, vol. 5, no. 10, pp. 823–829, 2006.

[20] J. F. Scott, “Room-temperature multiferroic magnetoelectrics,” *NPG Asia Materials*, vol. 5, no. 11, p. e72, 2013. [Online]. Available: http://www.nature.com/doifinder/10.1038/am.2013.58

[21] K. Arai, C. Muranaka, and M. Yamaguchi, “A new hybrid device using magnetostrictive amorphous films and piezoelectric substrates,” *IEEE Transactions on Magnetics*, vol. 30, no. 2, pp. 916–918, mar 1994. [Online]. Available: http://ieeexplore.ieee.org/lpdocs/epic03/wrapper.htm?arnumber=312444

[22] E. Lage, C. Kirchhof, V. Hrkac, L. Kienle, R. Jahns, R. Knöchel, E. Quandt, and D. Meyners, “Exchange biasing of magnetoelectric composites,” *Nature Materials*, vol. 11, no. 6, pp. 523–529, 2012. [Online]. Available: http://dx.doi.org/10.1038/nmat3306

[23] G. Lebedev, “Composites multiferoiques pour dispositifs magnetoelectriques integres,” Ph.D. dissertation, Universite de Grenoble, 8 2006.

[24] G. A. Lebedev, B. Viala, J. Delamare, and O. Cugat, “Voltage-Controlled Uniaxial Magnetic Anisotropy in Soft Magnetostrictive Ferromagnetic Thin Films,” *IEEE Transactions on Magnetics*, vol. 47, no. 10, pp. 4037–4040, oct 2011. [Online]. Available: http://ieeexplore.ieee.org/lpdocs/epic03/wrapper.htm?arnumber=6027792

[25] G. A. Lebedev, B. Viala, T. Lafont, D. I. Zakharov, O. Cugat, and J. Delamare, "Converse magnetoelectric effect dependence with CoFeB composition in ferromagnetic/piezoelectric composites," *Journal of Applied Physics*, vol. 111, no. 7, p. 07C725, 2012. [Online]. Available: http://link.aip.org/link/JAPIAU/v111/i7/p07C725/s1&Agg=doi

[26] J. D. Livingston, "Magnetomechanical Properties of Amorphous Metals," *Phys. Status Solidi*, vol. 70, pp. 591–596, 1982.

[27] G. A. Lebedev, B. Viala, T. Lafont, D. I. Zakharov, O. Cugat, and J. Delamare, "Electric field controlled magnetization rotation in exchange biased antiferromagnetic/ferromagnetic/piezoelectric composites," *Applied Physics Letters*, vol. 99, no. 23, p. 232502, 2011. [Online]. Available: http://link.aip.org/link/APPLAB/v99/i23/p232502/s1&Agg=doi

[28] A. I. Khan, X. Marti, C. Serrao, R. Ramesh, and S. Salahuddin, "Voltage-Controlled Ferroelastic Switching in Pb(Zr0.2Ti0.8)O3 Thin Films," *Nano Letters*, vol. 15, no. 4, pp. 2229–2234, 2015.

[29] S. Beguhn, Z. Zhou, S. Rand, X. Yang, J. Lou, and N. X. Sun, "A new highly sensitive broadband ferromagnetic resonance measurement system with lock-in detection," *Journal of Applied Physics*, vol. 111, no. 7, p. 07A503, 2012. [Online]. Available: http://scitation.aip.org/content/aip/journal/jap/111/7/10.1063/1.3671794

[30] E. R. Evarts, M. R. Pufall, and W. H. Rippard, "Continuous-film vs. device-level ferromagnetic resonance in magnetic tunnel junction thin films," *Journal of Applied Physics*, vol. 113, no. 8, p. 083903, 2013.

Supplementary Information

Analytical Basis

We designed the RF waveguide as a quarter-wavelength transformer, which resonates at a wavelength corresponding to 4× the length of the guide. The wavelength of a signal is defined by its frequency and the dielectric and magnetic properties of the medium through which it passes as given by the relationship:

$$\lambda = \frac{\nu_p}{f} \tag{7}$$

where ν_p is the phase velocity and is defined as

$$\nu_p = \frac{1}{\sqrt{\mu\epsilon}} \tag{8}$$

where μ is the magnetic permeability and ϵ is the dielectric permittivity of the medium. In free space, the phase velocity equals the speed of light; in a medium the wave propagation slows and the wavelength decreases. As a result of this change in the wavelength due to the material properties, the resonance frequency changes. Therefore, direct control of the material properties, specifically the permeability in the case of our work, allows for tuning of the resonant waveguide. Here, we utilize a magnetoelectric to provide electric field control of the magnetic permeability and tunability of the resonance frequency.

In our design, the coplanar waveguide sits on top of the magnetoelectric structure in order to observe the change in its radio frequency material characteristics, which provide the wireless tunable capabilities. As shown in the cross-section illustration in Fig. 6, the magnetic field circulates around the signal line as the wave propagates down the guide. With the magnetization oriented parallel to the length of the line, the magnetic field sees a hard-axis permeability along

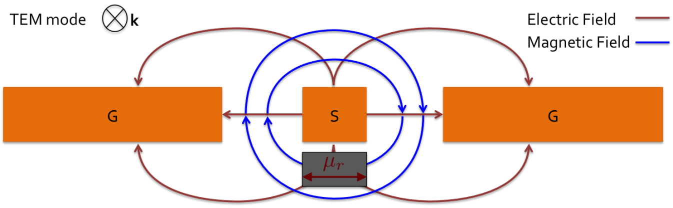

Figure 6: Cross-sectional diagram of the metal waveguide lines only, illustrating the electric and magnetic fields as the wave propagates down the guide.

the width of the guide below the signal line. When an electric field is applied to the piezoelectric and the magnet is stressed, the permeability will change and the change will be observable in the RF measurement results.

Due to the combined effect of laminations and strong shape anisotropy, the magnetization of the magnetic film is almost uniquely single domain, as shown in Fig. 5a of the main text, meaning that the magnetization will generally behave uniformly as a single rotating macrospin, without the presence of domain wall motion. (Furthermore, the macrospin assumption is particularly applicable in these experiments since we do not completely switch the direction of the magnetization and the magnetic film remains single domain under all applied electric field values.) Therefore, we assume macrospin analytical definitions to be valid for describing the magnetic anisotropy energies involved and utilize them for analysis of the magnetoelectric system.

By considering the magnetic anisotropy energies involved in the system, we can derive an expression for the stress required to completely rotate the magnetization by 90° [26,27] assuming only induced anisotropy (during deposition), shape anisotropy, and magnetoelastic anisotropy:

$$\sigma > \frac{H_k M_s + M_s^2(Ny - Nx)}{3\lambda_s} \sim \frac{H_{k_{eff}} M_s}{3\lambda_s} \quad \textit{in cgs units} \tag{9}$$

where σ is the stress, H_k and M_s are the induced anisotropy energy and saturation magnetization in cgs units, respectively, and N_y, N_x are the in-plane shape demagnetization factors (such that x is the easy axis direction along the length of the waveguide).

We measured the saturation magnetization of the film to be approximately $4\pi M_s \sim 17.4$ kG and the effective anisotropy field, folding into it the shape anisotropy, to be in the range of 80-100 Oe depending on the sample. Using these values, we approximate that the stress required to rotate the magnetization entirely is $\sim 66.9 - 83.6$ MPa. At a voltage of 150 V, COMSOL simulations suggest that an average tensile stress of ~ 150 MPa can be achieved in the film, implying that complete magnetization rotation may be possible. Moreover, while this calculation gives a good first-order approximation and suggests that the stress will be mostly tensile, the fabricated samples experience a more complicated stress arrangement, as discussed in the main text, which makes the response of the magnet harder to predict. In addition to the tensile stress, the film will experience compression in the two orthogonal directions. These stresses will also work to rotate the magnetization. However, most of these stresses are very localized near the electrodes (Fig. 4 of main text); the response of the magnetization to such localized stress is non-trivial to predict.

The FMR frequency can be approximated from the effective anisotropy field using the Kittel equation $\omega_{FMR} \sim \gamma\sqrt{H_{k_{eff}}(H_{k_{eff}} + 4\pi M_s)}$, where γ is the electron gyromagnetic ratio. For these samples, we expect the FMR frequency to fall between 3.3-3.7 GHz initially. The calculated $H_{k_{eff}}$ values from the FMR shift results correspond well with the previously determined anisotropy values from the hysteresis loop measurement.

We fabricated the coplanar waveguides to be 8mm long, such that the lowest frequency resonance would fall within the mobile frequency range between 1 - 3 GHz but below and well separated from the ferromagnetic resonance (FMR) frequency of the magnetic material. By operating below the FMR frequency, the magnetic permeability will still equal the film's low frequency value and the FMR resonance peak will not interfere with identification of the waveguide resonance frequency. The phase velocity of the propagating wave is calculated to be approximately $4.2 - 4.8 \times 10^7$ m/s, with quarter wavelength resonance frequency points between 1.3 - 1.5 GHz for the 8 mm-long waveguide. Despite the unique mechanical behavior of the poled devices under negative electric fields, the RF results agree very well with the predicted resonance frequency and permeability calculations.

Device Optimization

The ferroelectric structure at the bottom of the device was optimized using COMSOL Multiphysics simulation prior to fabrication. Given the stiff mechanical constraint of the structure due to substrate clamping, proper design of the electrodes was crucial in order to maximize the lateral tensile strain transferred to the magnetic material. Although a single set of interdigitated electrodes on either the top or bottom of the piezoelectric would offer more simplicity in fabrication, using two sets of electrodes (one on top and one on bottom) provides the most uniform lateral electric field distribution and therefore increases the corresponding horizontal strains by almost 20%.

The minimum electrode width was defined as 10 um due to fabrication constraints, but the pitch was optimized through simulation in order to balance the trade-offs involved: minimizing the "dead" regions and maximizing the electric field. The ferroelectric regions above/below the electrodes are considered "dead" regions since the electric field lines are not entirely horizontal and strains are not purely lateral in those areas. Therefore, increasing the density of electrodes also increases the density of dead regions and may not be desirable after a certain extent. Increasing the spacing between electrodes, on the other hand, reduces the strength of the electric field - defined as the voltage divided by the length of the field line - and reduces the strain, as a result. Nevertheless, increased spacing also means that the electric field lines are more horizontally oriented, making the strains more uniformly lateral. Given these tradeoffs, we achieve the maximum strain in this clamped magnetoelectric structure by keeping a 1:1 ratio of electrode width to electrode spacing.

Two generations of the magnetoelectric resonator devices were made. In the first, the top IDE were fabricated on the top surface of the PNZT and separated from the magnetic layer above by just a thin insulating oxide. This first generation device, however, suffered from dielectric breakdown between the top IDE and the conducting magnetic layer. To avoid dielectric breakdown at high fields, we designed a second generation device to include additional piezoelectric material above the top IDEs. This additional PNZT on top results in a less uniform electric field and strain distribution in that region, but resolves the breakdown issue. Fig. 5c of the main text shows successful poling of adjacent, oppositely-oriented domains between IDEs in the second generation device after application of a 1000 V pulse for a duration of 50 μs. The initially randomly oriented domains in the non-poled PNZT film become uniformly poled in opposite directions depending on the corresponding electric field directions produced by the electrodes.

Perhaps the most important question we sought to answer through simulation was whether a thin, 2.7 μm, PNZT film could produce sufficient stress in the magnetic layer to rotate the magnetization and change the permeability. Given that the piezoelectric film develops a strain under the applied electric field, the combined effect of the strain distribution across the layer, substrate clamping, and the mismatch of the elastic Young's modulus result in stresses to the magnetic material above it. Since we chose the CoFeB material for its high positive magnetostriction, the structure was designed such that the magnetization is originally orthogonal to the main strain axis and rotates towards it when a tensile (positive) stress is achieved. COMSOL simulations suggest that the net tensile strain at 150 V should be above the calculated stress level for magnetization rotation.

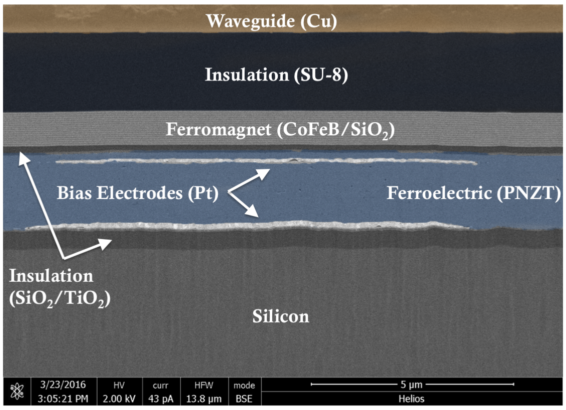

Figure 7: Focused ion beam cross-sectional image of the fabricated first generation device.

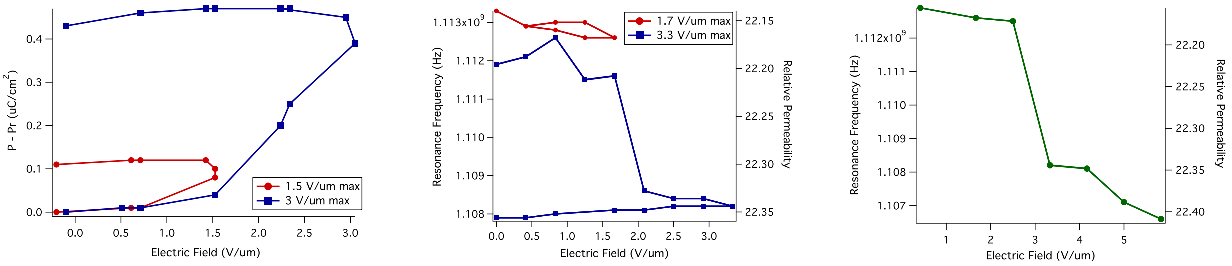

(a) (b) (c)

Figure 8: First generation device results: a) Polarization hysteresis loops as a function of electric field for the first iteration device. b) Quarter-wavelength resonance frequency sweep results as a function of electric field, described both in terms of frequency and permeability. c) Quarter-wavelength resonance frequency shift at increasing electric field steps. Results are described both in terms of frequency and permeability.

Generation 1 Device

In the first iteration of the magnetoelectric resonators, top and bottom IDE's sandwiched the piezoelectric layer, leaving only a thin insulation later separating the top electrodes from the conductive magnet (Fig. 7). Consequently, dielectric breakdown destroyed devices and limited the range of voltages that could be applied. Poling of the piezoelectric using high voltage pulses was not possible and all measurements were executed on the device beginning from its random, net-zero polarization state, similar to the PFM image of the non-poled region in Fig. 5b of the main text. When stepping voltage from the intial non-poled state, the resonance behavior appeared nonlinear and non-reversible as demonstrated by both the polarization versus electric field and resonance frequency versus electric field relationships in Fig. 8.

When an electric field is applied, the domains of the ferroelectric sporadically rotate to align with the field in a nonlinear fashion, depending on each domain's electrical coercivity [28]. Table 1 summarizes the strain and expected resonance behavior due to domain rotation for each initial domain configuration. As indicated by the strong contrast in the lateral PFM image, the majority of the ferroelectric domains are initially oriented in the plane. According to Table 1, this suggests that the predominant behavior is a downward shift in resonance frequency regardless of the initial domain orientation, which is seen from the RF measurement results of Fig. 8b. Figure 8c plots the resonance frequencies for the maximum voltage applied during each sweep; the decreasing trend confirms that the net behavior of the domains is lateral alignment and tensile strain.

While the general trend follows the expected decrease in resonance frequency with increased voltage, occasional temporary upward jumps in resonance frequency do occur. These, we expect, are due to a one or two-step rotation process involving the domains in the regions above and

Table 1: Summary of piezoelectric domain behavior and corresponding strains and resonance frequency shift depending on the intial state of the domain. Axes are labeled in parentheses.

Initial Polarization	Location	Final Polarization	Resulting Strains	Effect on $f_{\frac{\lambda}{4}}$
out-of-plane (z)	above/below electrodes	out-of-plane (z)	tension (z); compression (x,y)	no effect
	horizontally in between electrodes	in-plane (x)	tension (x); compression (z)	decrease
in-plane (y)	above/below electrodes	out-of-plane (z)	tension (z); compression (y)	decrease
	horizontally in between electrodes	in-plane (x)	tension (x); compression (y)	decrease
in-plane (x)	above/below electrodes	out-of-plane (z)	tension (z); compression (x)	increase
	horizontally in between electrodes	in-plane (x)	tension (x); compression (y,z)	decrease

below the electrodes. These domains may either be originally oriented along the x-direction and then rotate up/down to align with the out-of-plane component of the electric field in that region (one-step process); or, they are initially oriented along the opposite in-plane direction and first must rotate towards the x-direction, accompanied by a decrease in resonance frequency, then rotate out-of-plane, accompanied by a final increase in resonance frequency (two-step process). The slight contrast in the vertical PFM image above the electrodes indicates that the net polarization in those regions does indeed have a vertical component. This microscopic behavior qualitatively explains the occasional minor jumps in $f_{\frac{\lambda}{4}}$. Due to dielectric breakdown, this first generation of devices were limited in applied field range and could not be fully poled. We expected that once poled, the device behavior would be more linear and reversible. This hypothesis was verified with the second generation devices reported in the main text.